Resonance Raman Studies of Macrocyclic Complexes. 2. Antiresonance and Selective Intensity Enhancement in Synthetic Metal(II) Porphyrin Analogues

Laurence A. Nafie,* Richard W. Pastor, James C. Dabrowiak, and William H. Woodruff*

Contribution from the Department of Chemistry, Syracuse University, Syracuse, New York 13210. *Received April 30, 1976*

Abstract: The resonance Raman spectra are reported for the Mn(II), Cu(II), Ni(II), and Co(II) complexes of the dianonic N_4 macrocyclic ligand 5,7,12,14-tetramethyldibenzo[*b*,*i*][1,4,8,11]tetraazacyclotetradecahexenate (L^{2-}). Raman intensity patterns as a function of excitation frequency covering the argon ion laser emission lines (and the Rhodamine 6G dye laser emission region for $Ni^{II}L$) have been constructed. $Mn^{II}L$ and $Cu^{II}L$ show a simple one-term frequency dependence with the ligand $\pi \rightarrow \pi^*$ transition near 380 nm. $Ni^{II}L$ shows selective Raman intensity enhancement of low-frequency modes in resonance with a charge transfer band at 585 nm. Incontrast, the resonance behavior near the $\pi \rightarrow \pi^*$ transition shows characteristic enhancement of high-frequency ligand modes. In each region a one-term theoretical curve fits the data well. $Co^{II}L$ shows a strong antiresonance interference effect near 460 nm within a weak charge transfer band on the shoulder of the $\pi \rightarrow \pi^*$ transition. This is the first observation of Raman antiresonance involving only allowed electronic transitions. The data are fit with a two-term theoretical expression which demonstrates the origin of the antiresonance behavior. The interpretation of the Raman intensity patterns leads us to assign the 460 nm band in $Co^{II}L$ and the 585 nm band in $Ni^{II}L$ to charge transfer transitions and indicates that the 460 nm band is coupled to the ligand $\pi \rightarrow \pi^*$ transition while the 585 nm band is not.

The resonance behavior of Raman intensities as a function of the incident excitation frequency (excitation profiles) yields information concerning the nature of the resonant electronic transitions in relation to the vibrational modes of the molecular framework. Early experimental work involved primarily systems with only one resonant electronic state,[1-7] although this state may be vibronically coupled to a more distant nonresonant state. By considering only one resonant state, theoretical expressions are greatly simplified allowing comparison of various theoretical approximations to experimental results.[1,4-6] Recently, however, systems have been investigated which exhibit more complex resonance behavior owing to the direct influence of more than one resonant electronic state.[8-14] Some of these studies include the special case in which different vibronic levels of the same electronic state are considered as separate resonance states. Under multiple resonant state conditions features become possible which would otherwise be absent from the excitation profiles. One of these arises when the different resonant electronic transitions enhance different sets of vibrational frequencies. We refer to this effect as *selective Raman intensity enhancement.* Another effect is called *Raman antiresonance*[14] or Raman interference. This may arise when two or more electronic transitions enhance the same vibrational modes. Interference between these individual contributions may lead to unusual enhancement or deenhancement of the Raman bands as a function of incident frequency. Recently Stein et al.[14] have reported and explained theoretically the first observation of the Raman antiresonance effect,[15] although several papers have appeared which treat the subject theoretically.[8,16-18]

In this paper we report the detailed resonance behavior of a set of macrocyclic ligand complexes of the form $M^{II}L$, the structure of which is shown in Figure 1 of the previous paper[19] (to be referred to as paper 1), where M is either manganese, copper, nickel, or cobalt. In particular we demonstrate the presence of selective Raman intensity enhancement from different electronic states and report the first observation of antiresonance intensity deenhancement due to allowed electronic transitions.

Experimental Section

The Raman spectra were obtained by instrumentation described in paper 1. The intensities were obtained by measuring the peak areas with a planimeter. All areas were referenced to the area of the benzene solvent band at 606 cm^{-1}. The intensity data were then corrected relative to the reference band for absorption by the sample at the scattering wavelength, and response of the monochromator and photomultiplier, as well as the dependence of the intensity upon the fourth power of the scattered frequency. It was assumed that the benzene Raman peaks experienced negligible resonance enhancement in the excitation frequency domain of these experiments. Excitation profiles were then constructed by plotting these corrected intensity ratios vs. the laser excitation frequency. The complexes used in these experiments were synthesized and characterized as described in paper 1.

Results

The observed absorption spectra, excitation profiles for $Mn^{II}L$, $Cu^{II}L$, $Ni^{II}L$, and $Co^{II}L$, and the Raman spectra of $Ni^{II}L$ and $Co^{II}L$ are given in this section. The excitation profiles are accompanied by theoretical curves which show the correspondence of the data to a simple, one resonant electronic state expression. In each case the resonant electronic state is assumed to be the intense ligand-centered $\pi \rightarrow \pi^*$ electronic transition at approximately 380 nm.

Figure 1 contains the absorption spectra of $Mn^{II}L$ and $Cu^{II}L$. Only weak band shoulders and peaks on the low energy side of the $\pi \rightarrow \pi^*$ transitions appear in the near ultraviolet or visible regions of the spectrum. The excitation profiles of selected vibrational frequencies for $Mn^{II}L$ and $Cu^{II}L$ are shown in Figures 2 and 3. The experimental points for each of the different vibrational modes at a given excitation frequency are shown with their correct relative intensity values. The theoretical curve has the same form within each excitation profile and is scaled to give a least-squares fit to the data points for each vibrational mode. The form of the theoretical curves depends only on the location and bandwidth of the $\pi \rightarrow \pi^*$ transition in question. The theoretical description of these curves will be given in the next section.

The absorption spectra of $Ni^{II}L$ and $Co^{II}L$ are more complex than for $Mn^{II}L$ and $Cu^{II}L$ as shown in Figure 4. The prominent additional feature in the nickel spectrum is a band in the red centered at 585 nm which we assign as a charge transfer band. The $Co^{II}L$ spectra is even more varied with a series of four weaker bands ($\epsilon \sim 5000$ M^{-1} cm^{-1})[19] on the long wavelength side of the dominant $\pi \rightarrow \pi^*$ transition. The origins

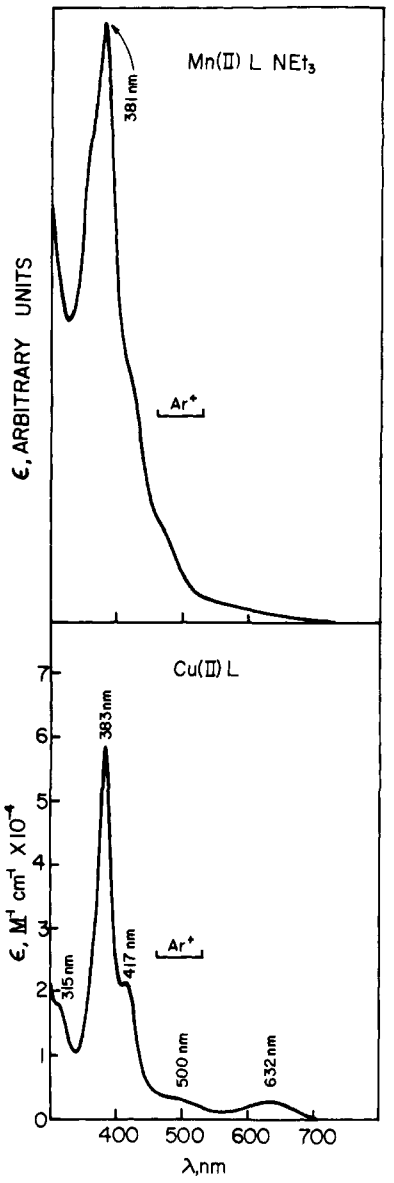

Figure 1. Absorption spectra of $Mn^{II}L{\cdot}NEt_3$ and $Cu^{II}L$ between 300 and 800 nm. The bar labeled Ar^+ indicates the wavelength range of the argon laser excitation lines.

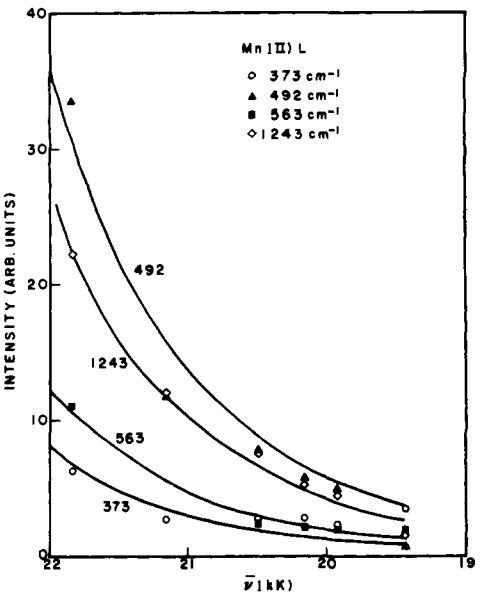

Figure 2. Raman excitation profiles for the 373, 492, 563, and 1243 cm^{-1} vibrations of $Mn^{II}L$. Each smooth curve represents a least-squares fit of eq 7 using ν_{eg} = 26 246 cm^{-1} (381 nm) and Γ_e = 1250 cm^{-1} to the experimental data points belnging to a given vibrational frequency.

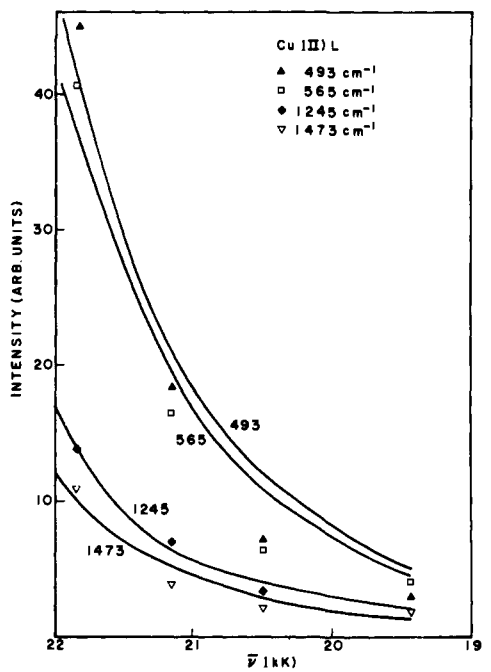

Figure 3. Raman excitation profiles for the 493, 565, 1245, and 1473 cm^{-1} vibrations of $Cu^{II}L$. Each smooth curve represents a least-squares fit of eq 7 with ν_{eg} = 26 110 cm^{-1} (383 nm) and Γ_e = 1390 cm^{-1} to the experimental data points belonging to a given vibrational frequency.

of these bands are again most likely charge transfer transitions. The resonance Raman spectra of $Ni^{II}L$ and $Co^{II}L$ at four typical argon ion laser frequencies are given in Figure 5, and Figure 6 contains the continuation of $Ni^{II}L$ spectra into the charge transfer band excitation region.

Excitation profiles for $Ni^{II}L$ in the two different excitation regions are given in Figures 7 and 8. These regions are also indicated in Figure 4 by a bar with either the designation Ar^+ or R6G corresponding to the region spanned by the argon laser lines or the dye laser region of Rhodamine 6G. The form of the theoretical curves used to fit the experimental points corresponds to a one-term expression associated with the 392 nm band in Figure 7 and the 585 nm band in Figure 8.

By comparing the Raman spectra taken at 457.9 and 472.7 nm in Figure 5 with the spectra at 590.4 nm in Figure 6 one can easily see that a different set of vibrational modes is enhanced in each case. Namely, the high-frequency ligand vibrations above 1200 cm^{-1} are enhanced in the blue near the ligand $\pi \rightarrow \pi^*$ transition while the low-frequency modes associated with the metal-ligand interaction are enhanced near the charge transfer band. The low-frequency vibrations at 568, 496, 391, 326, and 251 cm^{-1} appear to be enhanced in both excitation regions. The large band feature at the low-frequency end of the 590.4 nm spectrum in Figure 6 is due to fluorescence emission of the dye laser and not a vibrational transition. However, a vibrational band in $Ni^{II}L$ is observed at 200 cm^{-1} which is very strongly enhanced with dye laser excitation near the 585 nm absorption maximum. This mode was assigned to the metal-ligand stretch in paper 1.

The excitation profile for $Co^{II}L$ is given in Figure 9. A theoretical curve based on the 372 nm transition was used to fit the data points at the 514.5 nm (19 436 cm^{-1}), 501.7 nm (19 932 cm^{-1}), 496.5 nm (20 141 cm^{-1}), and 488.0 nm (20 492 cm^{-1}) laser lines. The data at 472.7 nm (21 155 cm^{-1})

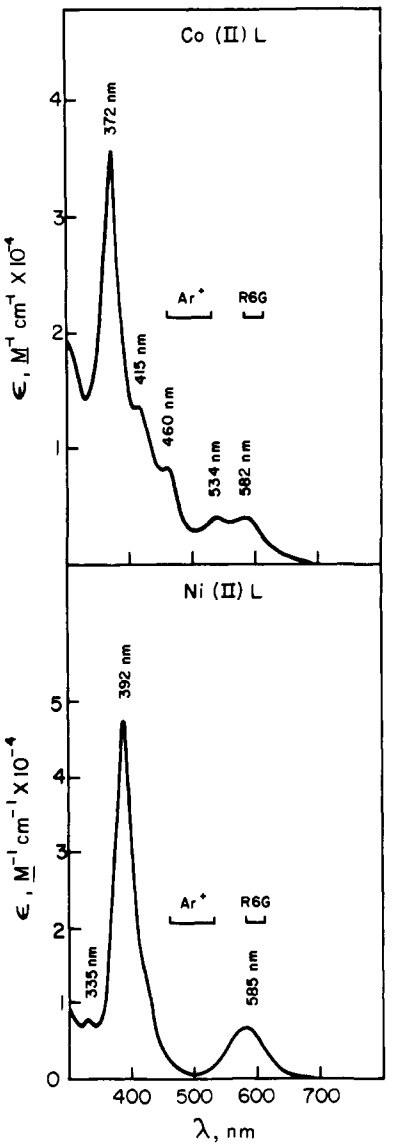

Figure 4. Absorption spectra of $Co^{II}L$ and $Ni^{II}L$ between 300 and 800 nm. The regions indicated by Ar^+ and R6G refer to the excitation regions of the argon laser lines and the dye laser with Rhodamine 6G dye, respectively.

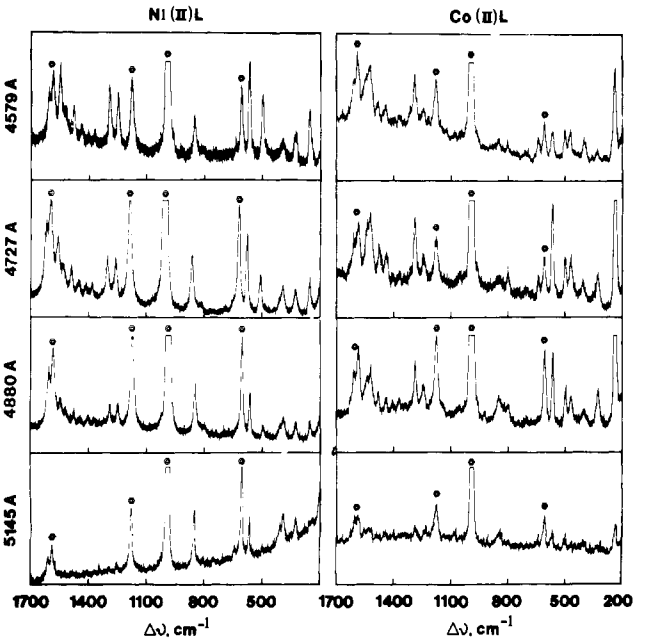

Figure 5. Resonance Raman spectra of $Ni^{II}L$ and $Co^{II}L$ using 4579 Å (21 838 cm^{-1}), 4727 Å (21 155 cm^{-1}), 4880 Å, (20 492 cm^{-1}), and 5145 Å (19 436 cm^{-1}) laser excitation. The benzene solvent peaks are indicated by hexagons.

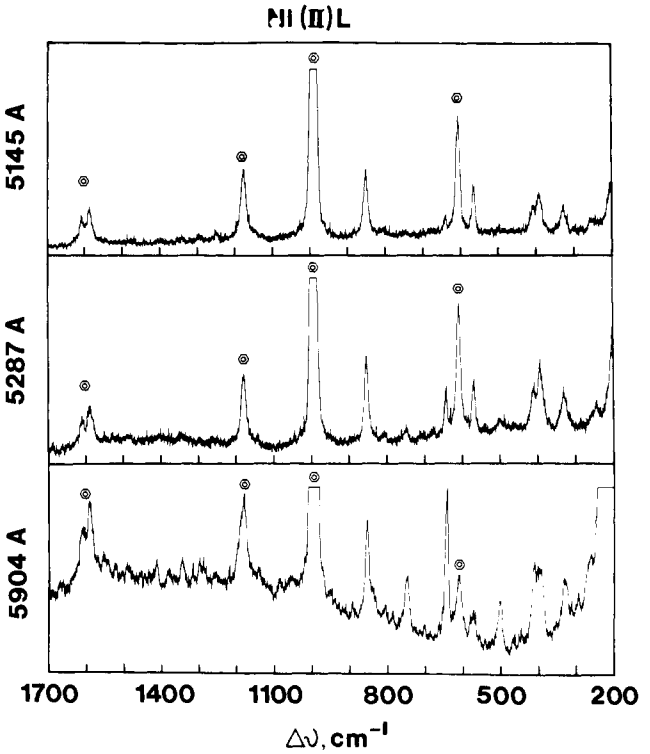

Figure 6. Resonance Raman spectra of $Ni^{II}L$ using 5145 Å (19 432 cm^{-1}), 5287 Å (18 914 cm^{-1}), and 5904 Å (16 937 cm^{-1}) laser excitation. The benzene solvent peaks are indicated by hexagons.

and 457.9 nm (21 838 cm^{-1}) fall respectively well above and below their theoretical curves indicating a systematic deviation from the simple one-term fit. Similar experimental patterns were obtained for the vibrations at 496, 1289, and 1476 cm^{-1} which for clarity were not included in Figure 9. The effect is quite striking in Figure 5 where virtually all the $Co^{II}L$ vibrations lose intensity relative to the benzene peaks from 472.7 to 457.9 nm, compared to the opposite behavior for $Ni^{II}L$ (which shows typical one-term resonance behavior) in the same figure. Another feature of interest in the $Co^{II}L$ spectra is the extreme enhancement of the cobalt ligand stretching vibration at 234 cm^{-1} within the 460 nm charge transfer shoulder.

Theory

The total intensity of a Raman transition after averaging over all orientations of the molecule is given in terms of the Raman tensor elements, $R_{\rho\sigma}$, by

$$I(\nu_r) = \frac{2^7\pi^5}{3^2c^4}\nu_r^4 I(\nu_0)\sum_{\rho\sigma}|R_{\rho\sigma}|^2 \qquad (1)$$

where ν_r is the frequency of the scattered light, c is the speed of light, and $I(\nu_0)$ is the intensity of the excitation laser beam at ν_0. Quantum mechanical expressions for the components of the Raman tensor have recently been given by Johnson, Nafie, and Peticolas[20,21] in a compact form which includes both Herzberg-Teller coupling and Born-Oppenheimer nonadiabatic coupling. According to these expressions, a transition between ground state vibrational levels gi and gj is given by

$$R_{\rho\sigma} = A + B \qquad (2)$$

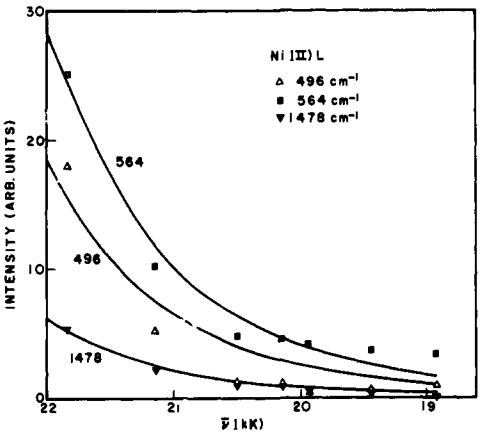

Figure 7. Raman excitation profiles of the 496, 564, and 1478 cm^{-1} vibrations of $Ni^{II}L$ using argon (Ar^+) laser excitation. Each smooth curve represents a least-squares fit of eq 7 with ν_{eg} = 25 510 cm^{-1} (392 nm) and Γ_e = 1320 cm^{-1} to the experimental data points belonging to a given vibrational frequency.

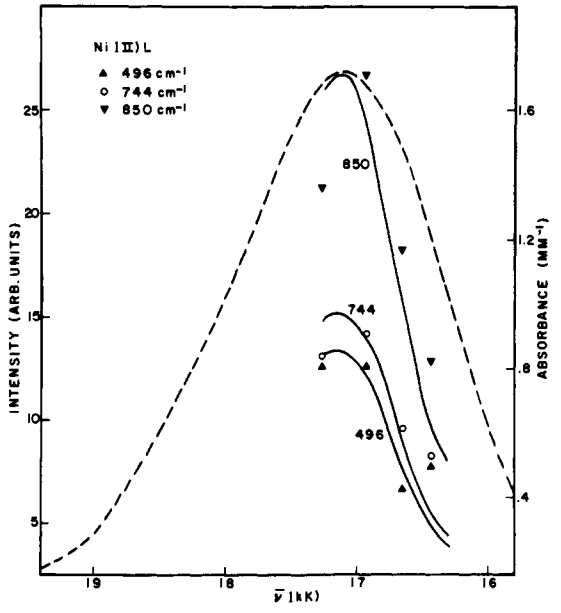

Figure 8. Raman excitation profiles of the 496, 744, and 850 cm^{-1} vibrations of $Ni^{II}L$ in the vicinity of the 585 nm absorption maximum (R6G dye laser excitation). Each smooth curve represents a least-squares fit of eq 7 with ν_{eg} = 17 100 cm^{-1} (585 nm) and Γ_e = 890 cm^{-1} to the experimental data points belonging to a given vibrational frequency. The dashed curve represents the absorbance per millimeter of the $Ni^{II}L$ Raman sample.

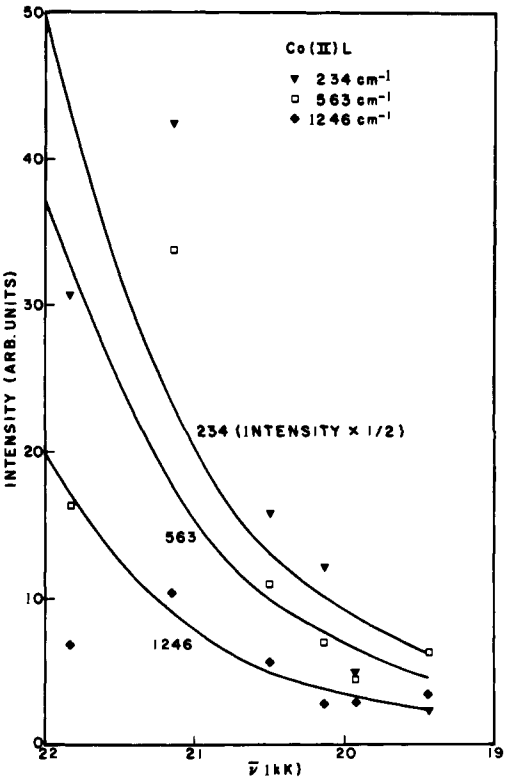

Figure 9. Raman excitation profiles of the 234, 563, and 1246 cm^{-1} vibrations of $Co^{II}L$. Each smooth curve represents a least-squares fit of eq 7 to the experimental data points for a given vibrational frequency obtained from laser excitation at 514.5 nm (19 436 cm^{-1}), 501.7 nm (19 932 cm^{-1}), 496.5 nm (20 141 cm^{-1}), and 488.0 nm (20 492 cm^{-1}). The values for ν_{eg} and Γ_e used in eq 10 are 26 880 cm^{-1} (372 nm) and 1370 cm^{-1}, respectively.

where

$$A = \frac{1}{h}\sum_{e,v}\left[\frac{(g^0|\mu_\rho|e^0)(e^0|\mu_\sigma|g^0)\,\langle gj|ev\rangle\langle ev|gi\rangle}{\nu_{ev,gi} - \nu_0 + i\Gamma_{ev}} + \frac{[\rho \leftrightarrow \sigma]}{\nu_{ev,gj} + \nu_0 + i\Gamma_{ev}}\right] \tag{3}$$

$$B = \frac{-1}{h^2}\sum_{e,v}\sum_{s,u}{}'\left[\frac{(g^0|\mu_\rho|s^0)(s^0|(\partial H/\partial Q)_0|e^0)(e^0|\mu_\sigma|g^0)\,\langle gj|su\rangle\langle su|Q|ev\rangle\langle ev|gi\rangle}{(\nu_{su,gi} - \nu_0 + i\Gamma_{su})(\nu_{ev,gi} - \nu_0 + i\Gamma_{ev})} + \frac{[\rho \leftrightarrow \sigma]}{(\nu_{su,gj} + \nu_0 + i\Gamma_{su})(\nu_{ev,gj} + \nu_0 + i\Gamma_{ev})}\right] \tag{4}$$

The eigenstates of the molecule have been divided into their electronic and vibrational parts, so that $|e^0)$ represents the adiabatic electronic wave function of the eth electronic state evaluated at the equilibrium nuclear position of the ground electronic state, and $|ev\rangle$ represents the vibrational wave function of the vth vibrational level of the eth electronic state. Subscripts which distinguish different vibrational modes have been omitted. The denominators have terms such as $\nu_{ev,gi} \equiv \nu_{ev} - \nu_{gi}$, the frequency separating vibronic levels, and damping constants Γ_{ev} which correspond to the inverse lifetime of the evth vibronic level. The vibronic coupling operator $(\partial H/\partial Q)_0$ is the change in the electronic Hamiltonian with normal mode displacement Q, evaluated at the equilibrium nuclear configuration of the ground state. The prime on the summation over s indicates the absence of terms where s equals e.

In order to reduce eq 2-4 to a form suitable to analyze the data in the excitation profiles we invoke the following simplifying assumptions. (i) Since the frequencies of all the electronic states to be treated theoretically are close to the frequency of the incident laser radiation, we neglect the nonresonant terms in eq 3 and 4 (i.e., those containing positive laser frequency terms, ν_0, in the denominator). (ii) Since vibronic detail cannot be seen in the smooth absorption bands in Figures 1 and 4, and furthermore since none of these bands has been identified to be vibronic in origin, we will invoke an approximation which eliminates or averages the vibronic detail of the resonant electronic states.

One such method for the A term, first outlined by Tang and Albrecht,[22] eliminates vibronic detail by expanding the frequency denominators about $\nu_e{}^0$, the frequency of the eth state evaluated at the equilibrium nuclear position of the ground state. However, this expansion does not converge close to resonance and is therefore not suitable here. An alternate approach recently published by Garozzo and Galluzzi[23] assumes identical, harmonic vibrational potentials for the ground and excited states having slightly different equilibrium nuclear positions. One then can express the excited state vibrational wave functions as a simple expansion in terms of the ground state vibrational wave functions. Inserting this expansion into the resonance term of eq 3 and considering only $0 \rightarrow 1$ vibrational transitions, one obtains

$$A = \frac{-1}{h^2} \sum_e \frac{(g^0|\mu_\rho|e^0)(e^0|(\partial H/\partial Q)_0|e^0)(e^0|\mu_\sigma|g^0)\ \langle g1|Q|g0\rangle}{(\nu_{eg}{}^0 - \nu_r + i\Gamma_e)(\nu_{eg}{}^0 - \nu_0 + i\Gamma_e)} \tag{5}$$

where Γ_e now refers to an average damping factor associated with the eth electronic state. A restriction on the use of eq 5 is that the shift in the equilibrium position of the eth state with respect to that of the ground state be small compared to the root mean square displacement of the nuclei in the lowest vibrational level of the ground state (i.e., $|Q_e{}^0 - Q_g{}^0| \ll \langle 0|(Q - Q_g{}^0)^2|0\rangle^{1/2}$). Although this condition is somewhat restrictive, it holds for many molecules and it is reasonable to expect that it applies in the present situation.

The B term can be simplified in a similar manner. Since the product of vibrational matrix elements is already first order in Q we need only consider the first term in the expansion of the excited state vibrational wave functions. This is equivalent to neglecting the small shift in the equilibrium positions of the potential wells associated with the ground and excited electronic states, and thereby making the excited state vibrational wave functions identical with the ground state vibrational wave functions. The constraint of a small equilibrium shift between the ground and excited state is still necessary for the convergence of the expansion of the excited state vibrational wave functions. The resonance term of eq 4 now becomes

$$B = \frac{-1}{h^2} \sum_e \sum_s \frac{(g|\mu_\rho|s^0)(s^0|(\partial H/\partial Q)_0|e^0)(e^0|\mu_\sigma|g^0)\langle g1|Q|g0\rangle}{(\nu_{sg}{}^0 - \nu_r + i\Gamma_s)(\nu_{eg}{}^0 - \nu_0 + i\Gamma_e)} \tag{6}$$

We note that eq 5 is exactly that portion of eq 6 which is excluded by the primed sum over s and hence these two equations may be combined into one expression having an unrestricted double summation over e and s. As pointed out by Garozzo and Galluzzi,[23] eq 5 and 6 are exactly the equations of Peticolas, Nafie, Stein, and Fanconi (PNSF)[24] and include both Herzberg-Teller coupling and Born-Oppenheimer nonadiabatic coupling.

In order to convert eq 5 and 6 to a form comparable in detail to the experimental excitation profile points we first set ν_r equal to ν_0 in the frequency denominators. This simplification is justified by the lack of vibronic detail in both the absorption spectra and the excitation profile points. It is equivalent to combining the 0-0 and 0-1 resonances of the PNSF equations into one resonance centered at the observed maximum of the absorption band envelope whose vibronic detail is not resolved. The approximation is particularly good for values of the damping constant that are comparable or larger than the Raman shift, where the individual 0-0 and 0-1 resonance peaks in the calculated excitation profile are not resolved. This condition appears to be consistent with the present experimental data; however, this approximation will be tested in the future when more detailed excitation profiles can be performed.

To obtain the total frequency dependence of the A and B terms we first consider only one resonant state, e, and one vibronically coupled state s. Then taking the absolute square of eq 5 and 6 and multiplying by the fourth power of the scattered frequency we obtain

$$F_A = \frac{\nu_r{}^4 a_e{}^2}{[(\nu_{eg}{}^0 - \nu_0)^2 + \Gamma_e{}^2]^2} \tag{7}$$

$$F_B = \frac{\nu_r{}^4 b_{es}{}^2}{[(\nu_{sg}{}^0 - \nu_0)^2 + \Gamma_s{}^2][(\nu_{eg}{}^0 - \nu_0)^2 + \Gamma_e{}^2]} \tag{8}$$

where a_e and b_{es} are the numerators in eq 5 and 6, respectively. Equation 7 represents the simple one resonant state frequency dependence used in the excitation profiles reported in the previous section. Values of $\nu_{eg}{}^0$ and Γ_e, obtained from the position and width of the absorption bands in Figures 1 and 4, were used to determine the form of eq 7 in each case.

We consider next the case when two resonant electronic states are important. In particular, three algebraically distinct expressions need to be considered, namely

$$F_{AA} = \nu_r{}^4|A_1 + A_2|^2 \tag{9}$$

$$F_{AB} = \nu_r{}^4|A_1 + B_2|^2 \tag{10}$$

$$F_{BB} = \nu_r{}^4|B_1 + B_2|^2 \tag{11}$$

where A and B refer to one resonant state expressions as in eq 5 and 6, respectively. The subscripts 1 and 2 refer to the to resonant excited states. F_{BA} is not distinguished from F_{AB} since the labels 1 and 2 are arbitrary. From the form of eq 9-11 it can be seen that the net contribution of the second resonant state may be negative if the cross-term is negative and larger in magnitude than the square of the smaller term. In the next section we show explicitly how this arises in the excitation profiles of $Co^{II}L$.

Discussion

Single State Resonance Behavior. The agreement between the experimental points for $Mn^{II}L$, $Cu^{II}L$, and $Ni^{II}L$ in the argon region and the theoretical curves derived from eq 7 is quite satisfactory. If the data had shown a more shallow enhancement as the laser excitation approached the $\pi \rightarrow \pi^*$ transitions, a B term as in eq 8 may have been more appropriate where the vibronically coupled state would be taken to be the next higher excited state. On the contrary, for some vibrational modes, the excitation profile points corresponding to the 488.0, 472.7, and 457.9 nm excitation wavelengths rise faster than the theoretical curve. This behavior is most likely due to weak sideband absorptions between 400 and 450 nm. However, the best one-term theoretical fit to the data is the A term of eq 7 using the frequency and half-width of the corresponding $\pi \rightarrow \pi^*$ transition. Similarly, the data for $Ni^{II}L$ in the dye laser region appear to be consistent with an A term fit with the 585 nm band, although we cannot absolutely rule out a B term expression with coupling to the $\pi \rightarrow \pi^*$ transition at 392 nm. Further data points in the region between 540 and 580 nm are required to settle this question with certainty, but the absence of resonance enhancement of high-frequency modes in the 585 nm band indicates no appreciable $\pi \rightarrow \pi^*$ character in this transition.

Raman Antiresonance in $Co^{II}L$. In order to describe the behavior of $Co^{II}L$ in the Ar^+ laser region, we need to select a two-term expression from eq 9-11. Since A term expressions satisfy the $\pi \rightarrow \pi^*$ resonance in the other metal(II) complexes, F_{BB} can be eliminated. Using the observed positions and half-widths of both the $\pi \rightarrow \pi^*$ transition and the weak sideband at 460 nm we have obtained theoretical curves using both F_{AA} and F_{AB}. The latter provides a far superior theoretical fit

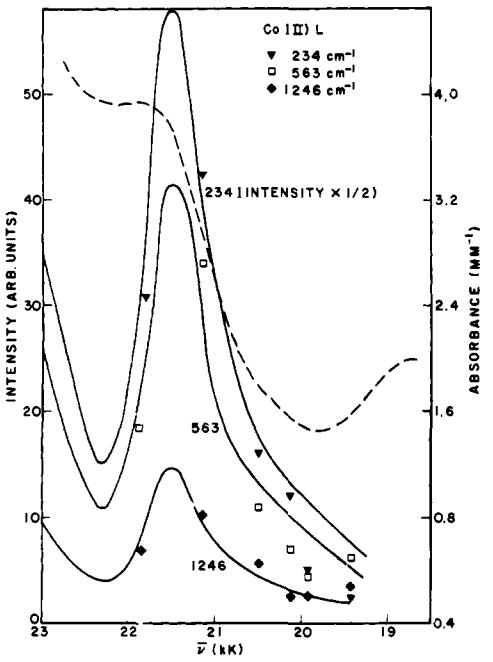

Figure 10. Raman excitation profiles of the 234, 563, and 1246 cm^{-1} vibrations of $Co^{III}L$. Each smooth curve represents a least-squares fit of eq 12 to the experimental data points for a given vibrational frequency, where ν_{1g} = 26 880 cm^{-1} (372 nm), ν_{2g} = 21 645 cm^{-1} (462 nm), T_1 = 1370 cm^{-1}, T_2 = 368 nm, a_1 = 91, and b_{21} = 7.3 [where the values of the quantities used in eq 15 are given in Table I]. The dashed curve represents the absorbance per millimeter of the $Co^{III}L$ Raman sample.

to the data, since F_{AA} weighted the resonance behavior of the sideband too heavily relative to the $\pi \rightarrow \pi^*$ enhancement. In addition F_{AA} provided only a small amount of antiresonance deenhancement near the sideband. Letting subscript 1 refer the $\pi \rightarrow \pi^*$ transition and 2 refer to the sideband near 460 nm, we employed the following expression,

$$F_{AB} = \nu_r^4 \left[\frac{a_1^2}{[(\nu_{1g}^0 - \nu_0)^2 + T_1^2]^2} + \frac{b_{21}^2}{[(\nu_{1g}^0 - \nu_0)^2 + T_1^2][(\nu_{2g}^0 - \nu_0)^2 + T_2^2]} + \frac{2a_1 b_{21}[(\nu_{1g}^0 - \nu_0)(\nu_{2g}^0 - \nu_0) + T_1 T_2]}{[(\nu_{1g}^0 - \nu_0)^2 + T_1^2]^2[(\nu_{2g}^0 - \nu_0)^2 + T_2^2]} \right] \quad (12)$$

To apply this expression to $Co^{III}L$ we took Γ_1 and Γ_2 to be the observed half-widths of the absorption bands and a_1^2, b_{21}^2, and $a_1 b_{21}$ to be proportional to the square of the intensity of the $\pi \rightarrow \pi^*$ transition, the squared intensity of the sideband transition, and the product of the intensities of the two transitions, respectively. The only approximation involved in this procedure is the original approximation of ignoring vibronic detail. In this approximation the intensities of the observed absorption bands are proportional to the expression for a_e and b_{es}.

A theoretical curve using eq 15 was calculated with the results shown in Table I where the intensity of F_{AB} has been normalized to unity at 514.5 nm. The columns headed term 1 and term 2 show the independent one-term resonance contributions of the $\pi \rightarrow \pi^*$ and the sideband transitions, respectively. The cross-term, which is in resonance with both of these transitions, first contributes heavily to enhancement and then to deenhancement of the overall intensity. The cross term becomes negative when $\nu_0 > \nu_{2g}^0 + \Gamma_1\Gamma_2/(\nu_{1g}^0 - \nu_0)$, which in this case can occur only after the excitation frequency becomes greater than the sideband transition frequency. We identify the antiresonance effect with the occurrence of a negative cross-term which results in a total intensity below the value of the individual one-term resonance contributions. This can be seen in Table I in going from λ_0 466.0 to 457.9 nm.

Table I. Calculated Values of F_{AB} in Equation 12 vs. Excitation Wavelength Normalized to F_{AB} = 1.00 at 514.5 nm[a]

λ_0, nm	Term 1	Term 2	Cross term	Sum
514.5	0.62	0.05	0.33	1.00
488.0	1.11	0.21	0.96	2.28
472.7	1.69	1.02	2.39	5.10
466.0	2.10	2.55	2.98	7.63
457.9	2.73	2.81	−1.20	4.34
450.0	3.65	1.19	−2.74	2.10
440.0	5.56	0.53	−2.73	3.36

[a] ν_{1g} = 26 880 cm^{-1}, ν_{2g} = 21 645 cm^{-1}, T_1 = 1370 cm^{-1}, T_2 = 368 cm^{-1}, a_1 = 91, b_{21} = 7.3.

The calculated total intensities of Table I were then scaled to a least-squares fit of the $Co^{III}L$ experimental intensities which resulted in the excitation profile curves of Figure 10. The absorption spectrum of $Co^{III}L$ in this region is included to provide a visual comparison between the Raman intensities and the visible spectrum. It is easily seen that a much better fit is obtained than the one-term expression used in Figure 9. Even so the experimental data are more strongly enhanced and deenhanced at 472.7 and 457.9 nm, respectively, than the two-term theoretical curve predicts. The data points further from resonance to the red suffer from the lower intensities resulting in greater experimental uncertainty as well as resonance enhancement from the bands at 532 and 584 nm.

An interesting feature of the observed antiresonance effect is that *all* the vibrational bands measured showed a sharp enhancement at 472.7 nm and a sharp deenhancement at 457.9 nm. This indicates that the weak band at 460 nm is not vibroni in *origin*, since vibronic bands show a progression of excitation profile maxima from low-frequency to high-frequency Raman modes, as is observed in the excitation profiles near the vibronic β band in ferrocytochrome *c*.[25] However, it can be concluded that unlike the $Ni^{II}L$ case, this sideband is vibronically *coupled* to the $\pi \rightarrow \pi^*$ transition owing to its *B* term frequency dependence in the two-term theoretical fit.

In Figure 5 it can be seen that the 234 cm^{-1} band assigned previously in paper 1 to the cobalt-ligand stretch is several times more strongly enhanced relative to the other vibrational modes in the vicinity of the 460 nm band. This lends support to the assignment of the 460 nm band to a charge-transfer transition. Furthermore, since the high-frequency ligand vibrations are also enhanced and deenhanced near this band, some $\pi \rightarrow \pi^*$ character must also be present. Otherwise these modes would be enhanced monotonically as the $\pi \rightarrow \pi^*$ transition at 372 nm was approached. This point then further supports vibronic coupling to the $\pi \rightarrow \pi^*$ transition in the 460 nm transition.

Selective Raman Intensity Enhancement. Finally we discuss the selective Raman intensity enhancement as observed in $Ni^{II}L$. Related phenomena have been reported, for instance, by Nafie et al.[9] and Strekas et al.[25,26] Both observed differential enhancement of Raman bands in different scattering regimes of heme proteins. In these cases the selective enhancement was due primarily to the symmetry and vibronic coupling properties of the resonant electronic states, so that depolarized and inverse polarized modes were enhanced in one region and polarized modes in another. Additionally, Strekas et al.[26] observed enhancement of certain high-frequency heme modes, which was thought to be due to charge-transfer resonance. Selective enhancement of metal-centered and ligand-centered vibrations has been observed in the excitation profiles of hemocyanin.[27] Recently Shelnutt et al.[13] have attempted to observe selective intensity enhancement of low-frequency metal-ligand vibrations in manganese(III) etioporphyrin I and

chromium(III) tetraphenylporphyrin chloride while in resonance with a band previously assigned as a charge-transfer transition. Failure to see such enhancement lead them to an alternate assignment for this band.

In the case of $Ni^{II}L$, as well as the other complexes, all the Raman bands are polarized, thus eliminating the symmetry of the resonant states as a selective mechanism. Second, *A* term theoretical curves adequately describe the excitation frequency dependence in both regions, thus making vibronic coupling an unlikely source of selectivity. Finally, the nature of the selectivity is to distinguish high- and low-frequency Raman modes, which correspond roughly to ligand vibrations at high frequency and to metal-ligand vibrations at low frequency. Since the high-frequency modes are enhanced near the ligand $\pi \rightarrow \pi^*$ transition and only low-frequency modes near the 585 nm transition one is naturally lead to assign the 585 nm band to a charge-transfer transition. In this way those modes are most enhanced which are most affected by the change in polarizability induced by the electronic transition.

Exceptions to the general arguments given above are noted by the enhancement of certain low-frequency ligand vibrations in the 585 nm band of $Ni^{II}L$ which are not assigned to metal-ligand vibrations. In particular the methyl C_a-C_b distortions at 496 and 564 cm^{-1} (see paper 1 for vibrational assignments) are enhanced with 590.4 nm excitation, as shown in Figure 6, and yet these vibrations are structurally well removed from the metal-ligand interface. This is also true for the enhanced phenyl associated vibrations at 747, 404, and 326 cm^{-1}, although the phenyl ring formally belongs to the conjugated electronic structure of the entire macrocycle, unlike the C_a-C_b bond of the substituent methyl groups. One might consider then the presence of considerable $\pi \rightarrow \pi^*$ character in the 585 nm transitions, but this may be discounted due to the absence of the high-frequency ligand vibrations which are enhanced only near the $\pi \rightarrow \pi^*$ transition. Some other coupling mechanism must then be responsible for the enhancement of the 496 and 564 cm^{-1} vibrations. It is unlikely that these vibrations contain substantial contribution from the metal-nitrogen stretching mode, due to the invariance in the frequency of the 496 and 564 cm^{-1} vibrations with the identity of the central metal ion (see paper 1). We suggest that instead the coupling mechanism is hyperconjugative in nature.[19] The C_b methyl groups can participate in the π delocalization of the macrocycle via a hyperconjugative resonance form. The magnitude of the contribution of such a resonance form is sensitive to the "π charge" on the delocalized structure.[28] In the present case, the ligand orbital which participates in the charge-transfer electronic transition (585 nm) is almost certainly a π orbital; therefore the π charge on the ligand differs between the charge-transfer ground and excited states of $M^{II}L$. Thus methyl group hyperconjugation must differ between the charge-transfer ground and excited states, and the normal coordinates associated with the C_a-C_b bond are uniquely affected by charge transfer transitions, whether ligand to metal or metal to ligand. We interpret the enhancement of the C_a-C_b vibrations in resonance with the 585 nm transition of $Ni^{II}L$ as evidence for such hyperconjugation, reflecting a large $\partial H/\partial Q$ for the charge-transfer transition with respect to the C_a-C_b related normal coordinates. A similar mechanism could lead to resonance enhancement of alkyl substituent vibrations in metalloporphyrins. This conclusion, deduced from empirical data, runs contrary to the recent theoretically based conclusion of Shelnutt et al.[13] that in porphyrins only vibrations containing a significant metal-nitrogen stretch contribution can be selectively enhanced upon excitation into a pure charge-transfer band.

Conclusion

From the analysis of resonance Raman scattering data presented above we have demonstrated the presence of two multiresonant electronic state features, namely antiresonance deenhancement and selective Raman intensity enhancement. The antiresonance behavior of $Co^{II}L$ was fit with a simplified two-term theoretical curve. This fit leads us to conclude that the 460 nm charge-transfer band is coupled to the $\pi \rightarrow \pi^*$ transition and is not a vibronic band whose origin is further to the red. The vibronic coupling conclusion is further supported by the absence of selective Raman intensity enhancement in the 460 nm charge-transfer band, since both metal- and ligand-centered vibrations are enhanced and behave in a similar manner. In $Ni^{II}L$ the nature of the selective Raman intensity enhancement suggests that the 585 nm band is charge transfer in origin and is not significantly coupled to the $\pi \rightarrow \pi^*$ transition. Enhancement of non(metal-ligand) low-frequency vibrations in $Ni^{II}L$ is attributed to hyperconjugative effects on the macrocyclic ring which are sensitive to the charge of the ligand π orbital participating in the charge-transfer transition.

Finally, we note that Shelnutt et al.[13] have concluded that it appears unlikely that charge-transfer bands will be observed to selectively enhance metal-ligand stretching vibrations in metalloporphyrins. On the basis of the present work with synthetic metal(II) porphyrin analogues we conclude that such enhancement, at least for certain metals, is quite possible and that its observation to date has been prevented by overlapping $\pi \rightarrow \pi^*$ transitions in the visible, or perhaps the lack of appropriate excitation frequencies. We suggest that the discovery of such charge-transfer bands in metalloporphyrins may be possible through the observation of "anomalous" selective intensity enhancement in the excitation profiles of low-frequency metal-ligand stretching vibrations, or conversely that the metal-ligand stretches can be identified by selective enhancement in resonance with charge-transfer transitions.

Acknowledgment. Acknowledgment is made to the donors of the Petroleum Research Fund, administered by the American Chemical Society, for support of this research. The authors also acknowledge an equipment grant from Syracuse University for construction of the Raman spectrometer and a Research Corporation Cottrell Grant (to W.H.W.) which made possible the purchase of the dye laser.

References and Notes

(1) A. C. Albrecht and M. C. Hutley, *J. Chem. Phys.*, **55**, 4438–4443 (1971).
(2) K. Kaya, N. Mikami, Y. Udagawa, and M. Ito, *Chem. Phys. Lett.*, **13**, 221–224 (1972).
(3) I. Suzuka, N. Mikami, Y. Udagawa, K. Kaya, and M. Ito, *J. Chem. Phys.*, **57**, 4500–4501 (1972).
(4) A. H. Kalantar, E. S. Franzosa, and K. K. Innes, *Chem. Phys. Lett.*, **17**, 335–341 (1972).
(5) A. Ranade and M. Stockburger, *Chem. Phys. Lett.*, **22**, 257–261 (1973).
(6) M. Tasumi, F. Inagaki, and T. Miyazawa, *Chem. Phys. Lett.*, **22**, 515–518 (1973).
(7) R. S. H. Clarke and P. D. Mitchell, *J. Am. Chem. Soc.*, **95**, 8300–8304 (1973).
(8) L. Rimai, M. E. Heyde, H. C. Heller, and D. Gill, *Chem. Phys. Lett.*, **10**, 207–211 (1971).
(9) L. A. Nafie, M. Pezolet, and W. L. Peticolas, *Chem. Phys. Lett.*, **20**, 563–568 (1973).
(10) D. W. Collins, D. B. Fitchen, and A. Lewis, *J. Chem. Phys.*, **59**, 5714–5719 (1973).
(11) J. M. Friedman and R. M. Hochstrasser, *Chem. Phys.*, **1**, 457–467 (1973).
(12) F. Galluzi, M. Garozzo, and F. F. Ricci, *J. Raman Spectrosc.*, **2**, 351–362 (1974).
(13) J. A. Shelnutt, D. C. O'Shea, N.-T. Yu, L. D. Cheung, and R. H. Felton, *J. Chem. Phys.*, **64**, 1156–1165 (1976).
(14) P. Stein, V. Miskowski, W. H. Woodruff, J. P. Griffen, K. G. Werner, B. P. Gaber, and T. G. Spiro, *J. Chem. Phys.*, **64**, 2159–2167 (1976).
(15) The authors are aware of unpublished work by A. Lewis on anomolous deenhancement in cytochrome *c*.
(16) O. S. Mortensen, *Chem. Phys. Lett.*, **30**, 406–409 (1975).
(17) J. Friedman and R. M. Hochstrasser, *Chem. Phys. Lett.*, **32**, 414–419 (1975).
(18) L. D. Barron, *Mol. Phys.*, **31**, 129–145 (1976).
(19) W. H. Woodruff, R. W. Pastor, and J. C. Dabrowiak, *J. Am. Chem. Soc.*, preceding paper in this issue.
(20) B. B. Johnson, L. A. Nafie, and W. L. Peticolas, *Chem. Phys.*, in press.

(21) W. L. Peticolas and B. B. Johnson, *Annu. Rev. Phys. Chem.*, in press.
(22) J. Tang and A. C. Albrecht, "Raman Spectroscopy", Vol. 2, H. A. Szymanski, Ed., Plenum Press, New York, N.Y., 1970, pp 33–68.
(23) M. Garozzo and F. Galluzzi, *J. Chem. Phys.*, **64**, 1720–1723 (1976).
(24) W. L. Peticolas, L. Nafie, P. Stein, and B. Fanconi, *J. Chem. Phys.*, **52**, 1576–1584 (1970).
(25) T. G. Spiro and T. C. Strekas, *Proc. Natl. Acad. Sci. U.S.A.*, **69**, 2622–2626 (1972).
(26) T. C. Strekas, A. J. Packer, and T. G. Spiro, *J. Raman Spectrosc.*, 1, 197–206 (1973).
(27) T. B. Freedman and T. M. Loehr, *J. Am. Chem. Soc.*, in press; *Biochem. Biophys. Res. Commun.*, **56**, 510–515 (1974).
(28) G. A. Olah and D. A. Forsyth, *J. Am. Chem. Soc.*, **97**, 3137–3141 (1975).

Structure Relationships between the Four-Coordinate, $S = 1$, Macrocyclic Complex, $[Fe(C_{22}H_{22}N_4)]$, and the Neutral Ligand, $C_{22}H_{24}N_4$

Virgil L. Goedken,*[1] Joseph J. Pluth, Shie-Ming Peng, and Bruce Bursten

Contribution from the Department of Chemistry, The University of Chicago Chicago, Illinois 60637. *Received March 3, 1976*

Abstract: Crystal and molecular structures of the, $S = 1$, four-coordinate iron(II) complex, 7,16-dihydro-6,8,15,17-tetramethyldibenzo[*b,i*][1,4,8,11]tetraazacyclotetradecinatoiron(II) and the isomorphous neutral ligand $C_{22}H_{24}N_4$ have been determined by three-dimensional x-ray crystallography. Pertinent crystal data are: space group, $P\bar{1}$; $[Fe(C_{22}H_{22}N_4)]$, $a = 9.429$ (2), $b = 11.401$ (3), and $c = 9.108$ (2) Å, $\alpha = 92.99$ (2), $\beta = 103.01$ (2), and $\gamma = 104.04$ (2)°; $C_{22}H_{24}N_4$, $a = 9.315$ (1), $b = 10.894$ (2), and $c = 9.928$ (1) Å, $\alpha = 96.53$ (1), $\beta = 107.04$ (1), and $\gamma = 101.53$ (1)° with $Z = 2$ for each compound. The ligands have a pronounced saddle-shaped conformation in each structure because of interactions of the methyl groups with the benzene rings. The overall conformations of the neutral ligand and the iron(II) complex are remarkably similar. A detailed structural interpretation of the free ligand is complicated by disorder involving degenerate tautomeric structures in the crystal lattice. The average Fe(II)–N bond distance of 1.918 (3) Å is significantly shorter than observed in $S = 0$ and $S = 1$ iron(II) porphyrin complexes. The donor electron pairs are directed slightly out of the N_4 coordination plane in each structure because of unequal tilting of the 2,4-pentanediiminato and benzenoid planes of the molecule. As a consequence, the Fe(II) atom is displaced 0.114 Å from the coordination plane.

Synthetic macrocyclic ligands have sufficiently diverse characteristics even among the fully conjugated systems to produce profound differences in the physical properties and reactivities of the coordinated metals. These differences are exemplified by the iron(II) complex $[Fe(C_{18}H_{18}N_6)(CH_3CN)_2]^{2+}$ (I), which shows no tendency towards oxidation by molecular oxygen,[2a] and the iron(II) complexes of the dianionic ligands of type II, which are exceedingly reactive toward molecular oxygen.[2b]

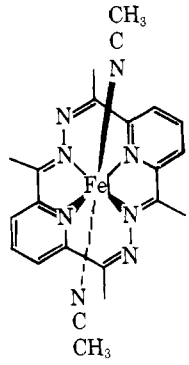

I

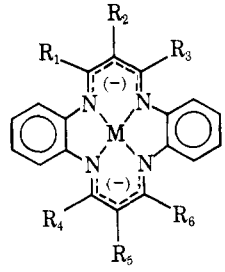

II

The metal–donor atom distance of a macrocyclic ligand is largely a function of the number of atoms in the macrocyclic ring and the extent of ligand conjugation. For example, the minimum strain M–N distance of 1,4,8,11-tetraazacyclotetradecane (cyclam), a 14-membered ring, and the free-base porphyrins which have 16-membered rings are similar, 2.07[3,4] and 2.04 Å,[5,6] respectively, because the contraction associated with a fully delocalized 16-membered ring compensates for the smaller number of atoms in the 14-membered ring. These values correspond well to commonly observed first-row transition-metal nitrogen distances. The completely conjugated 14-membered ligand, $C_{22}H_{22}N_4^{2-}$ (II, R_1, R_3, R_4, $R_6 = CH_3$; R_2, $R_5 = H$) is expected to have a much smaller radius than either cyclam or porphyrins because it has the equivalent of seven double bonds in a 14-membered macrocyclic ligand. Crystal structure analyses of three other completely conjugated 14-membered macrocyclic ligand complexes have revealed short metal–nitrogen distances (in the 1.80–1.90 Å range)[1,7-9] and illustrate the effect of extensive bond delocalization in these ligands on metal–nitrogen distances.

Significant departures from ideal metal–ligand bond lengths can considerably alter the properties of the resultant complexes. Small-diameter macrocyclic ligands can lead to unusually short metal–ligand distances, which are reflected in the redox potentials of the metal.[10] If the metal remains in the plane of the ligand, unusual electronic features may be observed. Alternatively, a constricting macrocyclic ligand may result in large displacements of the metal out of the ligand plane and lead to a preference for five-coordination. Large macrocyclic ligands with saturated rings of 16 or more atoms tend to be relatively unstable with respect to ligand dissociation and have weak ligand field strengths.[11] Unusual coordination numbers, for example seven-coordinate Fe(III), have been observed for some larger macrocyclic ligands.[12]

Transition-metal complexes derived from ligands of type II have been prepared and studied by a number of investigators with most of the studies confined to Ni(II),[13-16] although a few studies of complexes with Co(III),[17] Fe(II), Fe(III),[2] and Mo[18] have also been reported. The dianionic tetraaza ligands of II have a number of features in common with porphyrin and phthalocyanine ligands, but also have significant differences. Type II ligands, like the porphyrins and phthalocyanines, have